



HAL
open science

Wave Induced Motions of a Floating Mega Island

William Otto, Olaf Waals, Tim Bunnik, Coline Ceneray

► **To cite this version:**

William Otto, Olaf Waals, Tim Bunnik, Coline Ceneray. Wave Induced Motions of a Floating Mega Island. Chien Ming Wang; Soon Heng Lim; Zhi Yung Tay. WCFS 2019. Proceedings of the World Conference on Floating Solutions, 41, Springer, pp.173-189, 2019, Lecture Notes in Civil Engineering book series (LNCE), 978-981-13-8742-5. 10.1007/978-981-13-8743-2_9. hal-03028604

HAL Id: hal-03028604

<https://ensta-bretagne.hal.science/hal-03028604>

Submitted on 17 Jun 2021

HAL is a multi-disciplinary open access archive for the deposit and dissemination of scientific research documents, whether they are published or not. The documents may come from teaching and research institutions in France or abroad, or from public or private research centers.

L'archive ouverte pluridisciplinaire **HAL**, est destinée au dépôt et à la diffusion de documents scientifiques de niveau recherche, publiés ou non, émanant des établissements d'enseignement et de recherche français ou étrangers, des laboratoires publics ou privés.



Distributed under a Creative Commons Attribution 4.0 International License

Wave Induced Motions of a Floating Mega Island

William Otto, Olaf Waals, Tim Bunnik and Coline Ceneray

Abstract Floating mega islands can provide an attractive solution for creating temporal or more permanent space in coastal areas with a high demand for real estate. Also at open sea in the vicinity of wind farms, fish farms or logistical cross points, a floating mega island could be used as a hub, eliminating costly transfers. One of the aspects which needs to be understood is the wave induced motion of such a floating mega island. A piece-wise flexible island has been model tested at MARIN. The motion behavior in mild and severe sea states has been investigated. In this paper, the motion behavior is described and explained by comparing model test results with numerical simulations. An interesting aspect in this is the relative importance of wave diffraction, wave radiation and the dissipation of energy in the construction. The wave drift loads on the island that consists of 87 interconnected triangular pontoons are calculated and analyzed.

Keywords Mega-Floater motion behavior · Multi-body diffraction

1 Background and Applications

With an increasing population living mostly in coastal regions there is an increasing need for building space in coastal areas. Nowadays, this is mostly provided by land reclamation projects in densely populated areas, such as Singapore and the Netherlands. Some coastal regions also suffer from sea level rise and local subsidence of the soil. For example, in Jakarta additional measures have been taken to protect the city from the ocean. This paper discusses the possibility to use floating platforms as part of city development.

W. Otto (✉) · O. Waals · T. Bunnik
MARIN, Wageningen, Netherlands
e-mail: w.otto@marin.nl

C. Ceneray
ENSTA, Brest, France



Fig. 1 Village on lake Titicaca in Peru (left) and a fishery village in Ha Long Bay in Vietnam



Fig. 2 Left: A 1000 m floating runway in Tokyo bay, Right: Osaka Airport on reclaimed land

Also at open sea in the vicinity of wind farms, fish farms or logistical cross points, a floating mega island could be used as a hub, eliminating costly transfers. Mega islands can offer temporal or more permanent living and working space for:

- Developing, generating, storing, and maintaining sustainable energy
- Loading and transshipping cargo in coastal areas where there is little infrastructure;
- Cultivating food, such as seaweed and fish;
- Building houses and recreation close to the water.

The use of floating elements for living space is not new. There are small communities that have been living on floating islands for a long time. This is mostly in protected waters or on lakes. Two examples are shown in Fig. 1.

Floating constructions have been tested for large city infrastructures such as airports. One example is the 1000 m floating runway was tested in Tokyo bay [1]. In Japan, there is also a large experience with airport construction on reclaimed land (Fig. 2).

For city construction, one could list the most important design aspects as shown in Table 1. In this table, a comparison is made between the design aspects for a floating and a reclaimed island. Although there is much more experience with land reclamation projects the potential application area for floating islands is much larger.

Table 1 Design aspects

| Floating | Land Reclamation |
|--|--|
| <ul style="list-style-type: none"> • Relatively new technology • Motions • Larger water depth • Mooring loads • Risk of sinking • Design for tsunami • Cost • Impact on environment • Legal issues • Modular • Redeployable | <ul style="list-style-type: none"> • Proven technology • No motions • Limited water depth • Seawall loads • Risk of flooding • Design for earthquakes • Cost • Impact on environment • Legal Issues |

**Fig. 3** Artist impression of a large floating island

In limited water depths, one could also combine a fixed sea wall with a floating part. This has for example been done in the Semarang airport in Indonesia, where they are building a floating terminal as part of the airport extension.

Concepts for a floating city have been proposed by Quirk [2] and Roeffen [3]. These studies show the benefits of living at floating island by stipulating the risk of coastal flooding and the access to new sources of nutrition. Floating (air)ports consisting of an assembly flexibly connected modules have been studied by Kikutake [1] and Zhang [4], with the focus on a number of modules in the order of ~ 2 to 10. The response of very large flexible floaters has been investigated by Utsunomiya [5]. Murai [6] investigated the interaction with the local bathymetry.

Watanabe [7] has presented a concise literature overview of the work that was done on very large floating structures. A study on the effect of air cushions on the motions of large floaters was done by Van Kessel [8]. In the present study, we are investigating the response of coupled large triangular floaters. An artist impression is shown in Fig. 3.

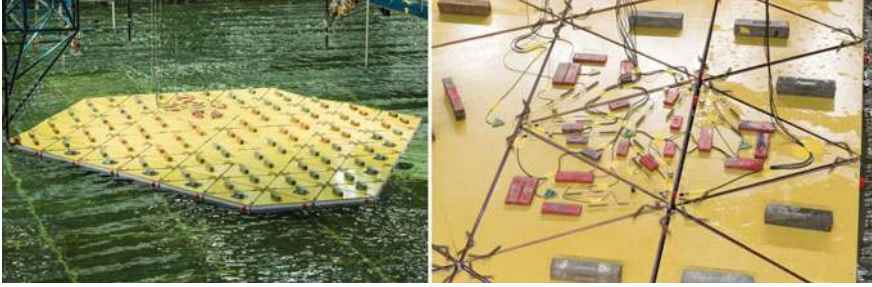


Fig. 4 Model of the floating island in the basin (87 modules)

2 Piecewise Flexible Island

In this paper the wave induced motions of a piecewise flexible island consisting of triangular rigid bodies are investigated. This island has been tested in MARIN's Offshore Basin as described by Waals et al. [9], see Fig. 4. For most of the applications of large floating islands it is a design objective to minimize the motions and building cost. In general the motions of floaters become smaller with increasing floater size. On the other hand larger floaters are more expensive and impractical to build. Very large floaters may show significant deflection and modal response and cannot be considered as one rigid body. Owing to the oscillating nature, the resulting strain may lead to local fatigue damage of the structure. By using a piecewise flexible floater the aim is to design the island such that the majority of the bending strain is in the connections between the modules. This reduces the internal loads in the island modules compared to a design where the mega structure is built in one piece. For the present island a system of interconnected triangular floaters was selected. The triangular shape was selected to restrict the least degrees of freedom of motion as possible for each individual floater. By connecting each pontoon on three sides an island surface is obtained that can bend in several directions. This allows for oblique wave conditions to pass the island with similar load levels as for the head on cases.

3 Wave Induced Motions

In [9], the motion Response Amplitude Operators (RAO's) of an 87 body linear diffraction calculation have been compared to the measured motions in the model scale tests. The initial comparison was poor. The authors suggest that the most likely explanation of the poor comparison is that the mechanical fenders and lines interconnecting the triangular modules were not taken into account in the numerical simulations. Also, the only source of damping was the wave radiation damping from potential flow. In order to better understand the numerical calculations, first a single body diffraction calculation was performed which is described in Sect. 3.1.

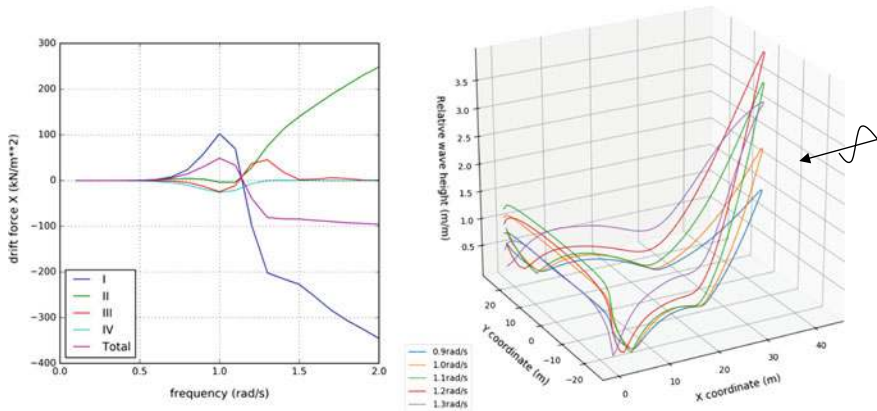


Fig. 5 Left, contributions to mean drift force on a single body triangle. Right, relative wave height along contour of triangle in unit wave amplitude

The improved results of the 87 body diffraction calculation is described in Sect. 3.2. A physical interpretation of the results is discussed in Sect. 3.3, the influence of the floater motions on the mean wave drift force of the assembly is discussed in Sect. 3.4.

3.1 Single Body Diffraction on Triangular Body

Before performing the diffraction calculation on the assembled island, a diffraction calculation was performed on one single triangle. These calculations showed interesting behavior in the drift forces. This is shown in Fig. 5 on the left for head waves, being waves traveling towards the point of the triangle. The total drift force is shown by the purple line, the four individual mathematical terms which add up to the total drift force are shown as well. It can be seen that around 1.0 rad/s, the sum of the drift force has a positive value. Physically, the interpretation of this is that the single triangle in waves is drifting towards the incoming waves. This peculiar result is counterintuitive compared to experience with other floaters and in the opinion of the authors unlikely for a blunt body in a viscous flow.

To better understand this behavior of the drift force, the four individual contributions to the mean drift are plotted as well. The full derivation of the four contributions can be found in [10], and the physical meaning is explained below;

- I = force due to first order relative wave elevation
- II = pressure drop due to the first order velocity
- III = force due to angular motion and inertia force
- IV = pressure due to gradient first order pressure and motion

As it can be seen, the peculiar drift force on a single body triangle in waves around 1 rad/s is mainly caused by the first contribution, which is associated with the relative

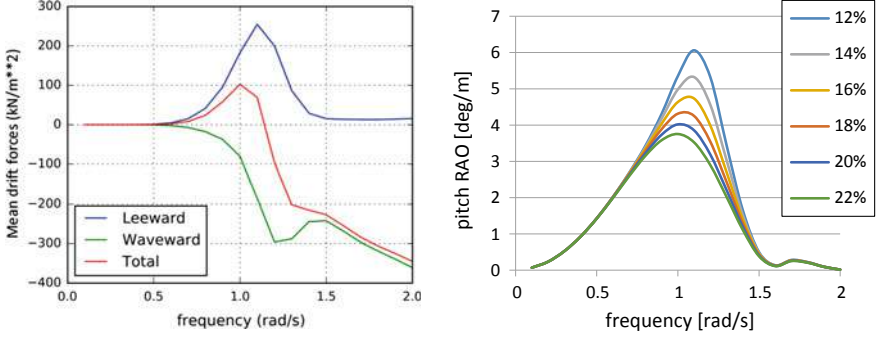


Fig. 6 Left, first contribution of mean drift force, Eq. (1) over waveward sides and leeward side. Right, pitch RAO for different values of critical damping

wave height along the module. Mesh sensitivity studies have shown consistent results for different mesh parameters. The relative wave heights are therefore plotted in Fig. 5 on the right for the relevant frequencies. It can be seen that the solution is smooth, and there are no discontinuities which might imply numerical instabilities. Note that the relative wave height is a result from the undisturbed wave, the diffracted wave, the radiated wave and the body motion, as calculated by the diffraction code. Given these relative heights, the first contribution of the drift force can be calculated by the integral of the relative wave height along the waterline WL (1);

$$F^{(2)} = -\frac{1}{2} \rho g \int_{WL} \eta_r^2 \vec{n} dl \quad (1)$$

In which η_r denotes the relative wave height and n the outward normal vector to the waterline. This equation applies to the waterline of all three sides of the triangle. Note that in X-direction, the normal vector of the two waveward sides have the same normal vector leeward of $+0.5$, the leeward side of the triangle has a normal vector of -1 . The integral over the two waveward sides are shown in green in Fig. 6 on the left, the integral over the leeward side is shown in blue.

It can be observed that the positive drift force is originating from the relative wave height at the leeward side of the triangle, the relative wave height is pushing the triangle at the leeward side against the wave. The relative wave height at this side of the triangle is mainly due to the motion response of the triangle, as the undisturbed wave and the diffracted wave are cancelling out each other to a great extent. The fairly straight lines in Fig. 5 on the leeward side of the triangle support this, the relative wave height at the leeward side is dominated by the pitch motion of the triangle. This leads to the hypotheses that the pitch response of the triangle is overestimated. Note that these calculations are performed with a potential flow method, without viscosity. The pitch response in reality is damped by radiation damping as well as by viscous damping. For this particular floater, the radiation damping around 1.0 rad/s is 12% of the critical damping. Additional linearised damping can be added to the diffraction

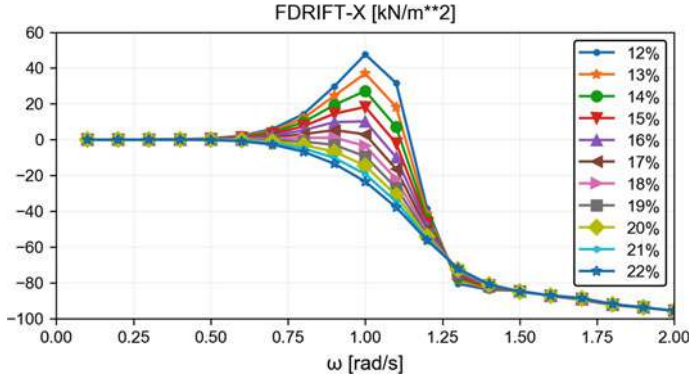


Fig. 7 Total drift force on single body triangle for different pitch damping values

calculation in order to allow for viscous effects. The sensitivity of added linear damping to the pitch motion RAO is shown in Fig. 6 on the right. It can be seen that for 12% critical damping (only radiation), the peak response is 6.0 deg/m, and drops to 4.5 deg/m for 18% of critical damping (6% viscous damping added). The sensitivity of the total mean drift force, the sum of all contributions, to the pitch damping is shown in Fig. 7. It can be seen that the positive drift force does not appear for damping levels higher than 18%, which corresponds to 6% added linearised viscous damping. Future work will show how realistic this is, by comparing the calculated motion response with single body model tests and, if feasible, viscous CFD calculations. When making this future comparison, it should be noted that viscous damping in general has a quadratic nature and care has to be taken on how to linearise it. For the present paper, it is assumed that adding 6% of linearised viscous damping is the most realistic but also most conservative scenario as this is the least amount of damping which needs to be added in order to eliminate the positive drift forces.

3.2 87-Body Motion Response Calculations

The motion response of the 87-triangle assembly is calculated in the frequency domain by using the results from a diffraction calculation as described in [9], a linearised viscous damping contribution as described in Sect. 3.1 and the stiffness and damping from the mechanical fenders and lines. The determination of the global stiffness matrix and damping matrix is a tedious task; their size is 522×522 (6 dof times 87 bodies), and they have contributions of not only the 87 floaters but also from the 256 fenders and 512 lines used to keep the assembly together. This makes their determination by hand not only time consuming but also prone to errors. In order to fill the damping and stiffness matrices in a convenient way a new functionality was added to aNySIM-XMF, which is an in-house MARIN tool dedicated

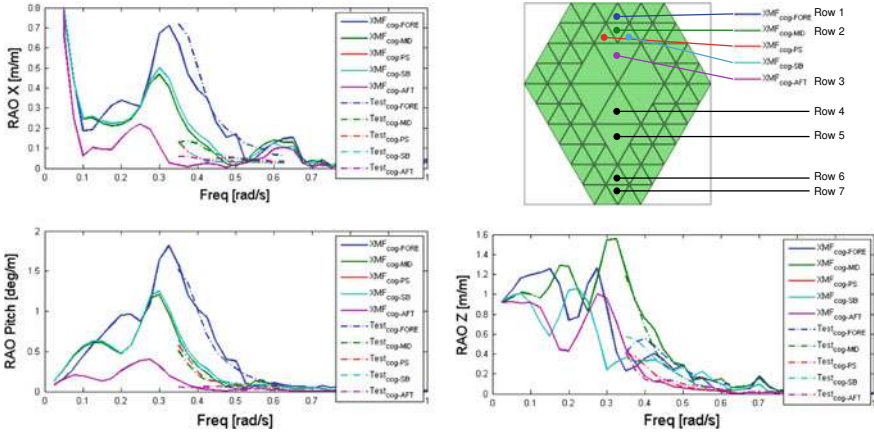


Fig. 8 Motion RAO of 87-body frequency domain calculation compared to model tests

to time domain simulations. By design aNySIM-XMF is a multi-body simulation tool in which mechanical joints and lines can be connected between n-number of bodies. Although designed for time domain simulations, the new functionality uses imposed motions to construct the stiffness matrix and imposed velocities to construct the damping matrix. Each body is consecutively moved by a small offset (1 mm in this case) and the resulting restoring force from all aNySIM components are stored in the linearised global stiffness matrix. This includes the hydrostatic as well as the mechanical restoring. Note that especially for the central triangles, a motion of one triangle results in a force on multiple others. The stiffness matrix therefore has a lot of non-diagonal interaction terms, in total 10,829 elements of the matrix are filled with non-zero entries. The damping matrix is filled in a similar manner.

The comparison between the calculated motion RAOs and those derived from the model tests as described in [9] is shown in Fig. 8. In general there is a good agreement between the tests and XMF calculations in the frequency range measured. During the tests, the motions of only five triangles were measured. Triangle denoted FORE is on the first row on the waveward side, the triangles MID, PS and SB are on the second row and AFT is the larger triangle on the third row. A trend of decreasing motion response when moving further away from the waveward row is clearly visible in the calculations as well as in the tests.

As it can be seen in Fig. 8, the frequency with the most response is around 0.325 rad/s. The motion response at this frequency is shown in Fig. 9. On the left is the real part of the motion RAO, which can be interpreted as a snapshot in time at t_0 , on the right the imaginary part of the motion RAO, which occurs $\frac{1}{4}$ wave period later. The phasing is with respect to the undisturbed wave at the CoG AFT, which is where the turret mooring is located in the tests as described in [9]. The colors represent the vertical motion, the horizontal motions are amplified 25 times in order

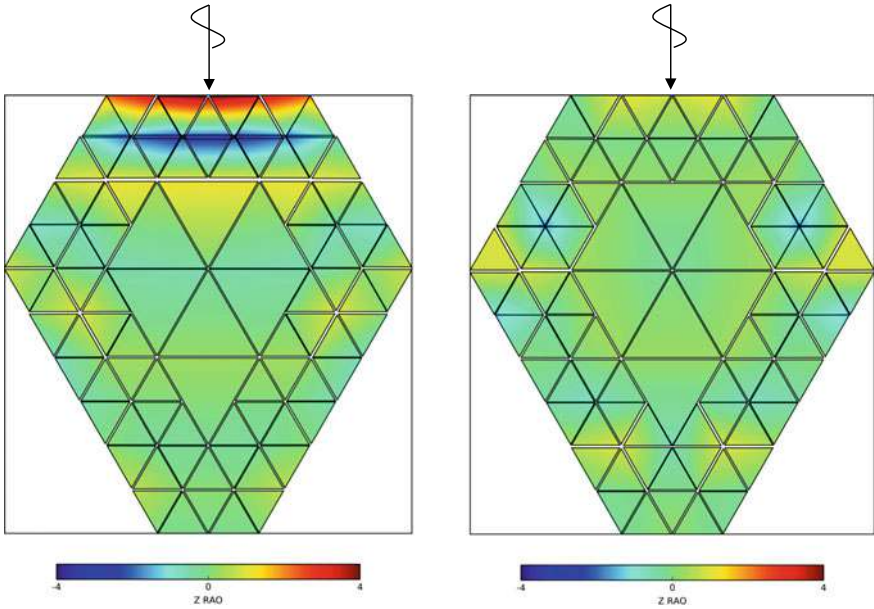


Fig. 9 Motion RAO at 0.325 rad/s of 87-body frequency domain calculation, horizontal RAO motions amplified 25 times. Real (left) and imaginary part (right)

to make them more visible. Note that because of this the first and second row on the waveward side are partially overlapping as there is compression in the fenders.

Although the motions of only five triangles were measured in the model tests, the video cameras confirm the general impression that the first and second rows on the waveward side move while the remainder of the assembly stays relatively still. This can be a convenient property for applications which have strict motion restrictions such as floating cities. In order to be able to design and optimize this behavior, the driving physics behind this are investigated in the next section.

3.3 Driving Physics Behind Motion Response

From both model tests and numerical calculations, the waveward triangles show the largest motion response and the response decreases when going further to the leeward side of the assembly. To better understand what is causing this behaviour, the pressure and response are plotted in Fig. 10. Note that in linear diffraction theory, the total wave field is reconstructed out of three wave fields; the undisturbed wave, the diffracted wave and the radiated wave. The wave excitation is defined as the resulting force of the combined undisturbed and diffracted wave field. On the top row of Fig. 10 the real part of the pressure fields and response are shown. As it can

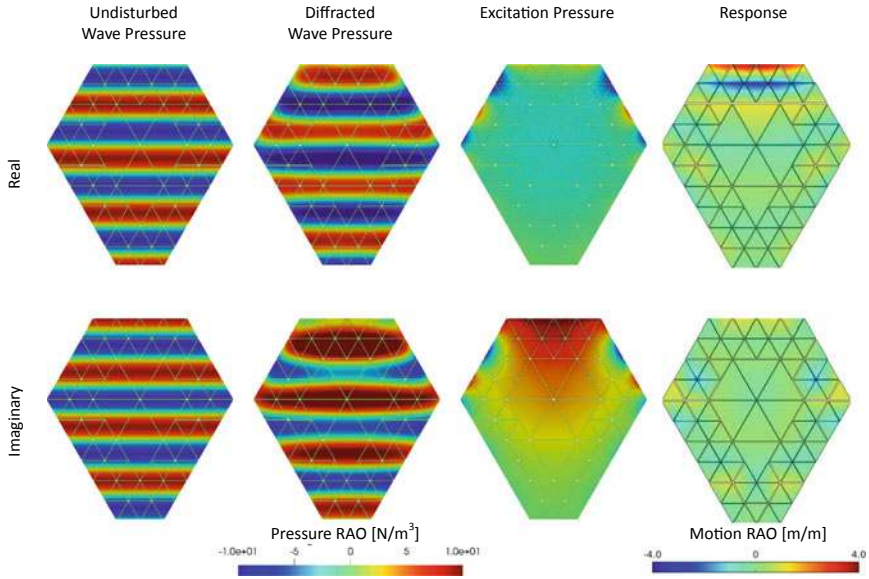


Fig. 10 Wave pressure and motion response per meter wave amplitude at 0.325 rad/s, top row real part, bottom row imaginary part, result of 87-body diffraction calculation

be seen, the undisturbed wave and the diffracted wave field are to a large extent in counter phase, cancelling out each other, which results in a reduced excitation. In the bottom row of Fig. 10 the imaginary part of the pressure fields are shown ($\frac{1}{4}$ wave period later than the real part). Here the diffracted wave is cancelling out the undisturbed wave only at the leeward side of the assembly. At the waveward side of the assembly, there is a net excitation force on the front.

The motion response is largely explained by the wave excitation, the first and second row of triangles on the waveward side have the largest motion response and also the largest wave excitation. Note that the response on the waveward side is mainly real, while the excitation is mainly imaginary. The phase lag between response and excitation is caused by the inertia of the structure. The wave excitation further to the leeward side of the assembly is decreasing to almost zero as the incoming wave is being diffracted by the first rows. It can be interpreted as that the leeward pontoons are sheltered by the waveward pontoons, the first two rows act like a wave deflector.

Another interesting overview is shown in Fig. 11. Here the calculated pitch and heave RAO of the central triangle of each row (see Fig. 8) is plotted. Around 0.275 rad/s, it is clear that the first two rows show the largest response, however the rows more to the leeward side also pitch and heave considerably. The wave excitation pressure at 0.275 rad/s is shown in Fig. 12. The wave excitation at this frequency shows a similar pattern as shown in Fig. 10, there is even less wave excitation at the leeward side at 0.275 rad/s than at 0.325 rad/s. Still the response at the leeward side around this frequency is larger as shown in Fig. 11.

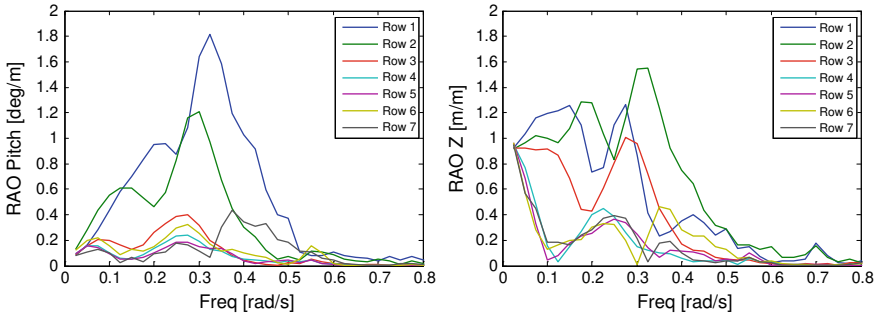


Fig. 11 Left; Pitch RAO Right; Heave RAO; central triangles of consecutive rows from full computation

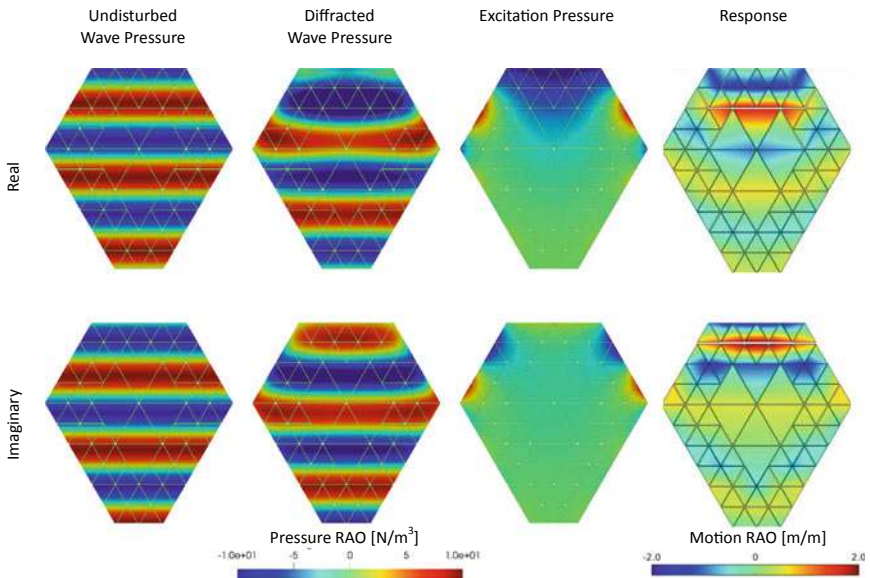


Fig. 12 Wave pressure and motion response per meter wave amplitude at 0.275 rad/s, top row real part, bottom row imaginary part, result of 87-body diffraction calculation

The response at 0.275 rad/s is also shown in Fig. 12. Behind the first two rows, a repetitive wave pattern becomes visible. It appears that the leeward side of the assembly is moving along with the undisturbed wave, despite the fact that the wave excitation indicates that the incoming wave is already diffracted at the waveward rows (the undisturbed wave is cancelled out by the diffracted wave). The contours of the motion response also show a bended, u-shaped profile in this plot.

In order to increase the understanding of this motion response, the same calculation has been performed without body interaction terms in the added mass and damping matrices. The physical meaning of this is that the force of a wave radiated

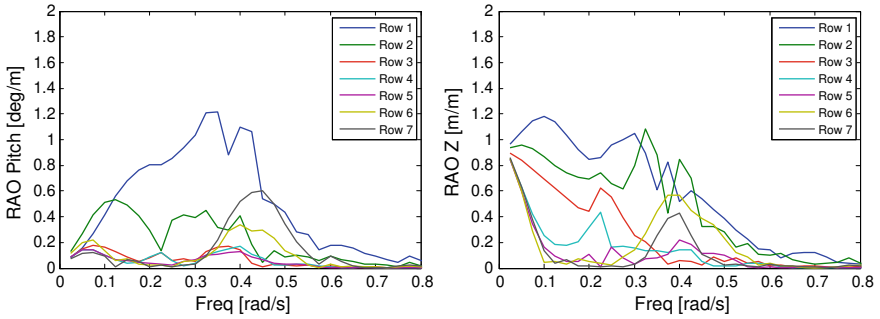


Fig. 13 Left; Pitch RAO Right; Heave RAO; central triangles of consecutive rows from computation without the radiating wave interaction between bodies

by a body is only felt by the body itself and not felt by the surrounding bodies. The resulting pitch RAO is shown in Fig. 13. It can be seen that the hump around 0.275 rad/s of the leeward rows (5, 6, 7) has almost disappeared.

Note that this plot has no further physical meaning. The only purpose of this plot is to investigate what is causing the response of these rows. It appears that at this particular frequency the leeward triangles are responding to the radiated waves from the waveward triangles. As radiated waves propagate in concentric circles, this might also be an explanation of the u-shaped contourlines in the motion plot. Note that these radiated waves are by definition caused by the motions of these bodies and they are proportional to their motion amplitude. In other words, the motions of the leeward triangles are hydrodynamically coupled to the motions of the waveward triangles by the radiated waves. This can be valuable insight when designing and optimizing a segmented island for a benign motion response, as the motions of the whole assembly can be altered by altering the motions of the first rows. This might for instance be done by varying the draft (inertia) of the triangles or by the stiffness of the connections. A sensitivity study of the motion response to these parameters will be part of future work.

Another interesting phenomenon in Fig. 11 appears around 0.45–0.50 rad/s. Although in general the response at this frequency is smaller than the response at lower frequencies, the last row shows a significant pitch response when compared to the first rows. The wave pressures and response at these frequencies are shown in Figs. 14 and 15. It is interesting to see that while at the frequencies 0.275–0.325 rad/s the excitation in the leeward islands was reduced to almost zero, the wave excitation at the leeward triangles around the frequencies 0.45–0.50 rad/s is in the same order of magnitude as on the waveward islands.

Further analysis of Figs. 14 and 15 shows that these excitation pressures are a result of the interference between the undisturbed and the diffracted wave. It seems that the diffracted waves form a frequency dependent pressure pattern underneath the island. The antinodes of this pattern is shown in the third picture from the left. The higher the frequency, the more complex the pattern becomes.

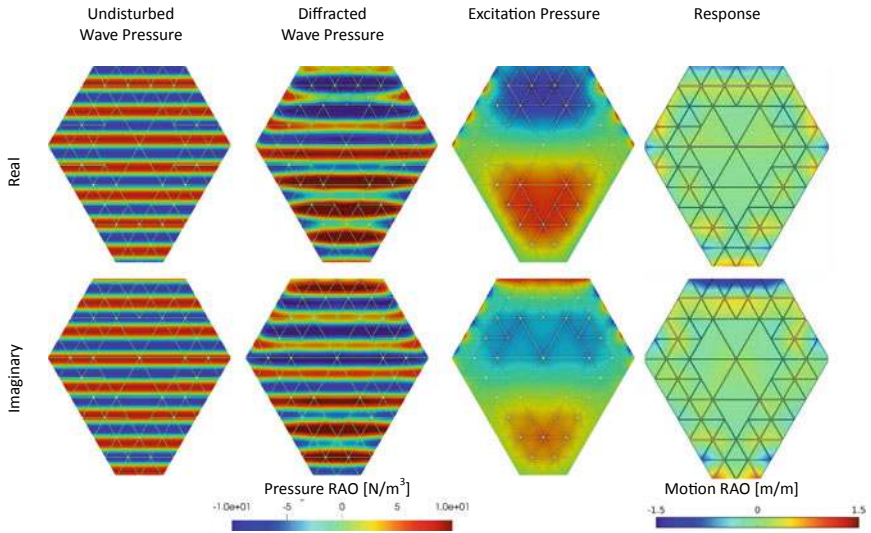


Fig. 14 Wave pressure and motion response per meter wave amplitude at 0.450 rad/s, top row real part, bottom row imaginary part, result of 87-body diffraction calculation

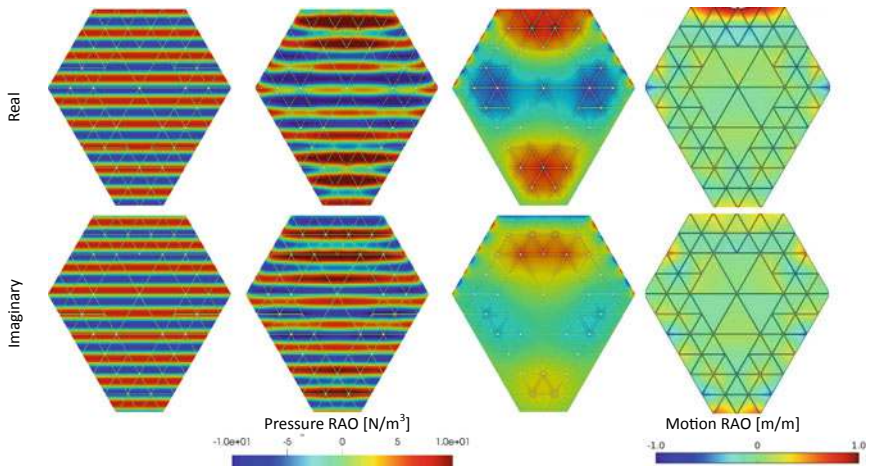


Fig. 15 Wave pressure and motion response per meter wave amplitude at 0.500 rad/s, top row real part, bottom row imaginary part, result of 87-body diffraction calculation

For this specific assembly the excitation at these frequencies does not lead to a large response because of the inertia of the individual modules. For design optimizations however this insight can be important when choosing the optimum ballast weight of the modules.

3.4 87-Body QTF Drift Forces

The first-order pressures, water velocities and motion responses resulting from the linear diffraction analysis can be used to compute Quadratic Transfer Functions (QTFs) for the mean and low-frequency wave drift forces using the direct pressure integration approach proposed by Pinkster [10]. In order to suppress unrealistic water motions in the gap between the triangles damping was added to the linearized free surface condition. In the frequency domain:

$$\frac{\partial}{\partial z}\varphi(\underline{x}) - (1 - i\varepsilon)\frac{\omega^2}{g}\varphi(\underline{x}) = 0 \quad (2)$$

This equation is enforced by panels on the free surface inside the gaps between the triangles. A damping value $\varepsilon = 0.03$ was used, which is based on experience with side-by-side offloading simulations, see Bunnik [12].

The wave drift forces are responsible for the mean offset and low-frequency motions of the island and are the governing the loads in the mooring lines. The drift forces on each individual triangle were computed. In this paper, only the mean drift force is considered. Figure 16 shows the surge wave drift force QTF on the entire island in head seas. The QTF has been computed with and without connection springs and added damping (see discussion in Sect. 3.2 on the effect of the motion response).

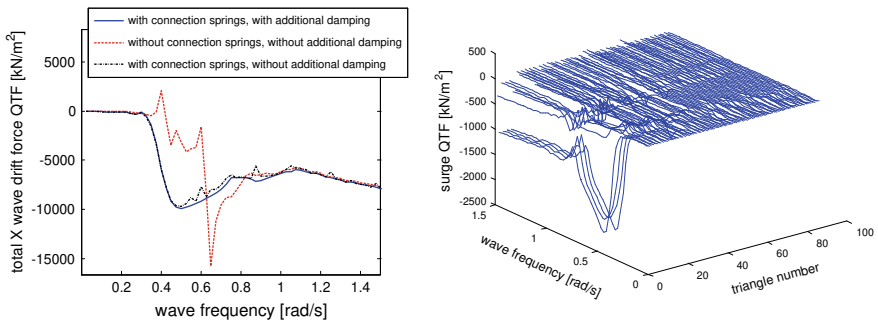


Fig. 16 Left; Mean surge wave drift force on all the 87 triangles combined. Effect of connection springs and added damping is shown. Right; Mean surge wave drift force on all the individual 87 triangles

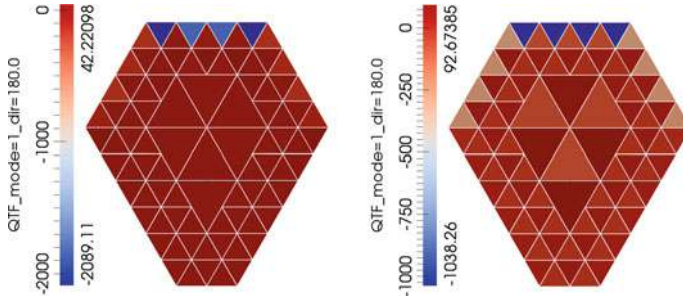


Fig. 17 Mean surge wave drift force per triangle. Left; 0.45 rad/s, Right; 1.25 rad/s

The effect of the connection springs on the QTF (through the motion response) is very large. The positive drift force disappears and the peak shifts to a lower frequency. The effect of adding the damping is to smooth the small oscillations that are present in the QTF. The connection spring and damping have no effect at higher frequencies because the triangles are not moving in short waves. The QTF is shown up to a frequency of 1.5 rad/s, which covers most of the wave energy of interest for the island. For higher frequencies, the present panel distribution was found to be too coarse to provide realistic results.

The mean drift force on each individual triangle is shown in Fig. 17 for two frequencies. For 0.45 rad/s, where the QTF is at a maximum, it can be seen that the drift force is mainly acting on the first waveward row. This insight can help in the design of mooring and connection, as the distribution of the loads is such that the leeward islands experience a benign drift force. The individual triangle with the largest positive drift force in this assembly is 42 kN/m², which is a small value compared to the largest negative value.

4 Conclusions and Further Work

In this paper, the wave induced motions of a piecewise flexible island consisting of 87 triangular rigid bodies have been investigated. This investigation is the first step towards a feasibility study of such a construction, with the obtained insights the safe operable limits and connection loads can be examined in future work. A linear diffraction method provided wave excitation and radiation values, the response is calculated in frequency domain with the incorporation of the mechanical connections in the global stiffness and damping matrix. Calculations on a single triangle led to the inclusion of an additional linear pitch damping in order to get realistic drift forces. For the assembly of 87 triangles, the calculated motion response shows a good similarity with the model tests for the triangles and frequencies measured.

Interesting wave interference patterns result in different motion response at different frequencies. At the frequencies with the largest motion response, the wave

excitation at the leeward modules is close to zero as the waveward islands diffract the incoming wave. This results in a benign motion response of the leeward islands, making those suitable for motion sensitive applications such as living. At slightly lower frequencies there is however motion response of the leeward islands, despite that there is no wave excitation acting on them. They are responding to the radiated waves of the waveward triangles. For higher frequencies the interference patterns result in wave excitation on both the waveward and leeward triangles. The motion response on this excitation is however small due to the inertia of the triangles.

The wave drift force has been calculated on the 87-triangle assembly as well. The drift force is sensitive to the motion of the triangles and therefore it is relevant to take the global stiffness and damping matrix, including mechanical connections, into account in the drift calculation. In this case, especially the stiffness matrix has a large effect on the drift force. The drift force is mainly acting on the waveward triangles, the leeward triangle experience almost no drift force.

Further work will include a more in-depth study to the viscous damping contribution on the triangles to better understand the assumptions in this paper. Also further work will be done to improve the wave response of the island by varying global design parameters such as draft, assembly shape, module shape and module size. As the present study shows that the waveward triangles are efficient in sheltering the leeward islands, the design optimizations could also include a separate breakwater, either floating or fixed.

Acknowledgements This project has received funding from the European Union's Horizon 2020 research and innovation programme under grant agreement No. 774253. The opinions expressed in this document reflect only the author's view and in no way reflect the European Commission's opinions. The European Commission is not responsible for any use that may be made of the information it contains.



References

1. Kikutake, T. (1998). A Mega-Float Airport, The State of the Art. In *Proceedings of the 17th International Conference on Offshore Mechanics and Arctic Engineering*, OMAE 1998. Lisbon, Portugal.
2. Quirk, J. (2017). *Seasteading: How ocean cities will change the world*. New York: Simon & Schuster.
3. Roeffen, B., Dal Bo Zanon, B., Czapiewska, K. M., & de Graaf, R. E. (2013). Reducing global land scarcity with floating urban development. In *Conference International Water Week*, Amsterdam.
4. Zhang, H. (2015). Nonlinear network dynamic characteristics of multi-module floating airport with flexible connectors. In *Proceedings of the 25th International Offshore and Polar Engineering Conference*, ISOPE2015, Kona, Hawaii, USA.

5. Utsunomiya, T., & Okafuji, T. (2006). Wave response analysis of a VLFS by accelerated Green's function method in infinite water depth. In *Proceedings of the 16th International Offshore and Polar Engineering Conference*, ISOPE2006, San Francisco, California, USA.
6. Murai, M., Inoue, Y., & Nakamura, T. (2003). The prediction method of hydroelastic response of VLFS with sea bottom topographical effects. In *Proceedings of the 13th International Offshore and Polar Engineering Conference*, ISOPE2003, Honolulu, Hawaii, USA.
7. Watanabe, E., Utsunomiya, T., & Wang, C. M. (2004). Hydroelastic analysis of pontoon-type VLFS: A literature survey. *Engineering Structures*, 26, 245–256.
8. Van Kessel, J. (2007). The effect of aircushion division on the motions of large floating structures. In *Proceedings of the 26th International Conference on Offshore Mechanics and Arctic Engineering*, OMAE2007, San Diego, California, USA.
9. Waals, O. J. (2018). Model tests and numerical analysis for a floating Mega Island. In *Proceedings of the ASME 2018 37th International Conference on Ocean, Offshore and Arctic Engineering*, OMAE1018, Madrid, Spain.
10. Pinkster, J. (1980). Low frequency second order wave exciting forces on floating structures. PhD thesis, TU Delft.
11. Utsunomiya, T., Watanabe, E., & Nakamura, N. (2001). Analysis of drift force on VLFS by the near-field approach. In *Proceedings of the 11th International Offshore and Polar Engineering Conference*, ISOPE2001, Stavanger, Norway.
12. Bunnik, T. (2009). Hydrodynamic analysis for side-by-side offloading. In *Proceedings of the 19th International Offshore and Polar Engineering Conference*, ISOPE2009, Osaka, Japan.